Temperature- and frequency-dependent optical and transport conductivities in doped buckled honeycomb lattices

Andrii Iurov, Godfrey Gumbs, and Danhong Huang

Phys. Rev. B **98**, 075414 — Published 13 August 2018

DOI: 10.1103/PhysRevB.98.075414

Temperature- and frequency-dependent optical and transport conductivities in doped buckled honeycomb lattices

Andrii Iurov[1*], Godfrey Gumbs[2,3], and Danhong Huang[4]

[1]*Center for High Technology Materials, University of New Mexico, 1313 Goddess SE, Albuquerque, NM, 87106, USA*

[2]*Department of Physics and Astronomy, Hunter College of the City University of New York, 695 Park Avenue, New York, NY 10065, USA*

[3]*Donostia International Physics Center (DIPC), P de Manuel Lardizabal, 4, 20018 San Sebastian, Basque Country, Spain*

[4]*Air Force Research Laboratory, Space Vehicles Directorate, Kirtland Air Force Base, New Mexico 87117, USA*

(Dated: July 30, 2018)

* Corresponding author's email: aiurov@unm.edu

Abstract

Thermal and dynamical properties of optical and transport conductivities in doped buckled honeycomb lattices are studied for various doping densities and bandgaps. At finite temperatures, a thermally-convoluted polarization function is calculated by employing analytically derived temperature-dependent chemical potentials. With this finite-temperature polarization function, the optical conductivity, originating from an induced polarization current, is obtained in the long-wavelength limit, where both steps and negative peaks are shown as a function of frequency in its real and imaginary parts, respectively. Such spectral features can be used for analyzing plasmon dampings in silicene and ultrafast light modulations based on field-tunable bandgaps. Additionally, in the presence of static screening, derived with the aid of the polarization function, for impurity elastic scattering, the transport conductivities are calculated for different doping densities and bandgaps within the second-order Born approximation. The enhanced transport conductivity with a smaller bandgap at intermediate temperatures will lead to high-mobility electron transistors for ultrafast electronics.

PACS numbers: 72.10.Fk, 71.45.Gm, 73.20.Mf, 73.21.-b

I. INTRODUCTION

The successful mechanical exfoliation of groups-IV and V layered materials has spurred a substantial amount of interest in two-dimensional (2D) materials in condensed matter physics [see Ref. 1 and other references therein]. Their planar or buckled structures, lattice asymmetry, nanoscale thickness as well as their stacking configurations cause these 2D materials to possess some unusual physical and chemical properties. This causes some of them to have interesting electronic, optoelectronic and spintronic device applications. Other buckled group-IV hexagonal 2D lattices include germanene [2–8] and others. Free-standing germanium allotropes had been previously predicted to be stable, low-buckled honeycomb structures with a much larger bandgap ($\backsim 23.9\, meV$) opened by spin-orbit coupling (SOC). Experimentally determined linear V-shaped density-of-states (DoS) provides strong verification for a gapped Dirac dispersion relation in germanene. [9]

The Hamiltonians used to model these buckled-lattice systems need to take into account the effect of SOC and interlayer atomic interactions. While graphene and silicene are two representatives of these established 2D materials, sharing many similar electronic properties due to a hexagonal lattice, [10–13] the unique silicon-based 2D Kane-Mele topological insulator, [14] however, has a relatively large spin-orbit bandgap ($\backsim 1.55\, eV$) which could be nearly doubled under an external strain. [15,16] The bandgap is associated with sublattice asymmetry and leads to a tunable energy band structure in the presence of an external electric field, [15,17–25] enabling potential applications to ultrafast light modulation with a high extinction ratio for ultra-wideband digital communications. All these effects can be attributed directly to a finite out-of-plane buckling caused by a larger ionic radius of a silicon atom compared to carbon and by the sp^3 hybridization of electronic orbitals [17,21] at the same time. These interesting bandgap properties also offer tremendous advantages to controlling a current flow because electrons could be effectively confined by electrostatic gate voltages yielding variable potential barriers. More importantly, these silicene-based devices are compatible with silicon wafer processing in manufacturing silicon-based integrated circuits. Compelling experimental evidence for the existence of such graphene-like lattices while putting down the synthesis of epitaxial silicene sheets on silver is shown and discussed in Ref. [15].

There have been a number of key reports on silicene's thermal conductivity and transport coefficients, [26–28] molecular dynamics studies, [29] first-principle calculations of electron-

phonon coupling and its effects on electron mobility,[30] unusual thermoelectric behavior in Rashba spintronic materials,[31] inhomogeneous quantum critical fluids,[32] effects of anisotropy in phosphorenes,[33] and detailed Monte Carlo studies[34].

The works in Refs. [35] and [36] presented detailed fundamental studies of AC- and DC-transports in buckled honeycomb lattices, including the calculations of spin and charge currents for individual valley, investigation of the thermo-spin effect, and modification of Kubo formalism by adding an effective magnetization to their model. It has been shown that the spin- and valley-Hall conductivities exhibit a strong temperature dependence. Another theoretical paper[37] on quantum spin and valley Hall effect was devoted to a spin-separation process by valley-Hall effect in the absence of a magnetic field, which could be important for potential device applications. A study on optical response of silicene and other low-buckled structures under an electron doping was reported in Ref. [38] and demonstrated a strong dependence of its conductivity on a field-induced bandgap.

In a pioneering work Ref. [39], analytic calculation for the conductivity of free-standing graphene in the frequency and wave vector domains was performed at various temperatures. It was demonstrated that for each chosen temperature range, a simple analytical expression for the conductivity could be derived.[40] At low enough temperatures and carrier concentrations, the inter-band contribution is shown to play a leading role.

In previous times, the semiclassical Boltzmann transport theory has been extensively used for hot electrons in semiconductor quantum-wire systems beyond the relaxation-time approximation[41–43]. Boltzmann transport in the presence of scattering by ionized impurities has been investigated thoroughly for graphene for a low bias field,[44–46] demonstrating agreement between theory and available experimental data[47,48]. Carrier transport was also studied in bilayer graphene[49] and in low-density silicon inversion layers.[50]

However, the combined effects due to doping and finite temperatures on the electron transport in buckled honeycomb lattices with two diverse energy subbands and bandgaps have not been explored extensively and will be chosen as the principal focus here.

The rest of our paper is organized as follows. We first briefly introduce the low-energy Hamiltonian and obtain associated electronic states in Sec. II for buckled honeycomb lattices. For doped silicene, we study the chemical potential at an arbitrary temperature using linear DoS for a wide class of gapped Dirac structures[51]. Applying the random-phase approxima-

tion (RPA), we further compute in Sec. III the dynamic polarization function and discuss its limiting behaviors at either small wavevectors or low frequencies, which become crucial in determining optical [52] and transport [53] conductivities, respectively. In Sec. IV, both the optical- and transport-conductivity calculations are performed, along with displayed numerical results, in the long-wavelength limit for incident light and within the screened second-order Born approximation for elastic scattering. For silicene, there exist two inequivalent subbands and both intra- and inter-subband impurity scatterings are considered for energy-relaxation time of doped electrons. Finally, our concluding remarks providing an overview are provided in Sec. V.

II. LOW-ENERGY ELECTRONIC STATES AND CHEMICAL POTENTIAL

We begin this section by exploiting previously reported band-structure models for low-energy electronic states of buckled honeycomb lattices. We first consider silicene as an example, but keep in mind that similar properties, e.g., constant internal spin-orbit bandgap (Δ_{SO}) and field ($\mathcal{E}_\perp$) dependent sublattice-asymmetry bandgap $\Delta_z \sim \mathcal{E}_\perp$, as well as two inequivalent subbands, could also be applied to germanene.

The low-energy dispersion relations for a buckled honeycomb lattice, obtained from a block-diagonal Hammiltonian matrix, [17,25] have been shown to be

$$\varepsilon^{\gamma}_{\xi,\sigma}(k) = \gamma\sqrt{\left(\xi\sigma\Delta_z - \Delta_{SO}\right)^2 + \left(\hbar v_F k\right)^2} \equiv \varepsilon^{\gamma}_{\beta}(k) \ , \tag{1}$$

where $\boldsymbol{k} = (k_x, k_y)$ is a 2D wavevector of electrons, v_F the Fermi velocity, $\sigma = \pm 1$ a real spin index and $\xi = \pm 1$ a valley index. From these dispersions we obtain two symmetrical subbands for electrons ($\gamma = +1$) and holes ($\gamma = -1$), respectively. Here, each subband in Eq. (1) is specified by its two gap parameters $\Delta_{<,>} = |\Delta_{SO} \mp \Delta_z|$, depending only on the composite indexes $\beta = \xi\sigma$. This composite index β will be used throughout this paper.

It is evident that both band gaps $\Delta_\beta = \Delta_{<,>}$ depend on $\mathcal{E}_\perp$ through Δ_z. By increasing $\mathcal{E}_\perp$ from zero, $\Delta_<$ is reduced, which corresponds to a topological-insulator state for $\Delta_z < \Delta_{SO}$. When $\Delta_z = \Delta_{SO}$, we find $\Delta_< = 0$ for the lower gap. This unique state is referred to as the valley-spin polarized metal (VSPM) [17,25]. If $\Delta_z > \Delta_{SO}$, we return to the standard band-insulator (BI) phase.

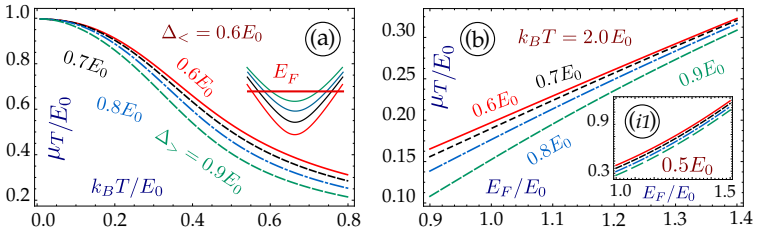

FIG. 1: (Color online) Silicene μ_T dependence on T and E_F. Panel (a) shows μ_T as functions of k_BT for $E_F/E_0 = 1$, $\Delta_</E_0 = 0.6$, and $\Delta_>/E_0 = 0.6$ (red solid curve), 0.7 (black short-dashed), 0.8 (blue dash-dotted), 0.9 (green dashed). Plot (b) displays μ_T as functions of E_F for $k_BT/E_0 = 2$ and $k_BT/E_0 = 0.5$ (inset). Here, colors and types of various curves for different Δ_β are defined in the same way as in (a).

In performing numerical calculations, energies and frequencies will be given in units of an energy scale $E_0 = 5.22\,\mathrm{meV}$, which corresponds to a gapless-graphene electron doping density $n_0 = 1\times 10^{11}\mathrm{cm}^{-2}$. Here, the wavenumber is in units of $k_0 = E_0/\hbar v_F$, and the Fermi energy $E_F = E_0$ will be always assumed unless it is stated in figure captions for cases with varied E_F.

The silicene band structure in Eq. (1) gives rise to the following piecewise linear density-of-states (DoS) [36,38,54]

$$\rho_d(\varepsilon) = \frac{\varepsilon}{\pi\,(\hbar v_F)^2}\sum_{\gamma=\pm 1}\sum_{\beta=<,>}\Theta\left(\varepsilon/\gamma - \Delta_\beta\right)\ , \tag{2}$$

where $\Theta(x)$ is the Heaviside step function, accounting for unavailable electronic states within the lower gap, as illustrated schematically in Fig. 6(a). Equation (2) can be employed to determine E_F at zero temperature ($T = 0$) with a fixed carrier density n_c, leading to [51,55]

$$2\pi(\hbar v_F)^2\, n_c = \begin{cases} E_F^2 - \Delta_<^2 & \text{for } E_F < \Delta_>\ , \\ 2E_F^2 - (\Delta_<^2 + \Delta_>^2) & \text{for } E_F > \Delta_>\ . \end{cases} \tag{3}$$

Here, the upper subband is occupied only for $n_c \geq 2\Delta_{SO}\Delta_z/\pi\hbar^2 v_F^2$, which corresponds to the second line in Eq. (3).

Moreover, the T-dependent chemical potential μ_T, which equals to E_F at $T = 0$, can be decided from the conservation of carrier numbers in thermal-equilibrium states. The details about the derivation of μ_T can be found from Ref. [51], which yields [51,54,56]

$$\pi\left(\frac{\hbar v_F}{k_BT}\right)^2 n_c = \sum_{\beta=<,>}\sum_{\gamma=\pm1}\left[-\mathrm{Li}_2\left(-\mathsf{e}^{\frac{\gamma\mu_T-\Delta_\beta}{k_BT}}\right)+\frac{\Delta_\beta}{k_BT}\,\ln\left(1+\mathsf{e}^{\frac{\gamma\mu_T-\Delta_\beta}{k_BT}}\right)\right]\gamma\,, \qquad (4)$$

where $\mathrm{Li}_2(x)$ is a polylogarithm function, and n_c is related to E_F by Eq. (3). From Eq. (4) we find that μ_T depends on both T and E_F, as shown in Fig. 1, and the dependence is controlled by energy gaps $\Delta_<$ and $\Delta_>$. Furthermore, we find significant difference in μ_T at low and intermediate T. For $k_BT \ll E_F$, Eq. (4) reduces to previous approximate results. [57,58]

III. OPTICAL-POLARIZATION FUNCTION

We now turn our attention to an investigation of the dynamical polarization function $\Pi_T(q,\omega\,|\,\mu_T,\Delta_\beta)$ for n-doped silicene at arbitrary temperature. The function $\Pi_T(q,\omega\,|\,\mu_T,\Delta_\beta)$ is recognized as one of the most important quantities in characterizing optical properties of an electronic system. In order to account for screening effect on a Coulomb potential between two electrons, we use a dielectric function $\epsilon_T(q,\omega)$, which, under the random-phase approximation (RPA), takes the form

$$\epsilon_T(q,\omega) = 1 - v(q)\,\Pi_T(q,\omega\,|\,\mu_T,\Delta_\beta)\,, \qquad (5)$$

where $v(q) = 2\pi e^2/\epsilon_s q$ is the 2D Fourier-transformed Coulomb potential, and $\epsilon_s = 4\pi\epsilon_0\epsilon_b$ with ϵ_b as the background dielectric constant in which the 2D material is embedded. In Eq. (5), zeros of $\epsilon_T(q,\omega)$ determine the dispersion $\omega_{pl}(q)$ of plasmon excitations. [59,60] For silicene, these plasmon modes become spin- and valley-polarized and they also rely on an external electric field. [61] The full optical-polarization function is a sum [25] of two results for gapped graphene [60]

$$\Pi_T(q,\omega\,|\,\mu_T) = \sum_\beta \Pi_T(q,\omega\,|\,\mu_T,\Delta_\beta)\,, \qquad (6)$$

which depends on μ_T, $\Delta_<$ and $\Delta_>$.

In the one-loop approximation, the dynamical polarization function in Eq. (6) at finite T is given by

$$\Pi_T(q,\omega\,|\,\mu_T,\Delta_\beta) = \sum_{\gamma,\gamma'=\pm1}\int\frac{d^2\boldsymbol{k}}{2\pi^2}\,\mathcal{F}_{\gamma,\gamma'}(\boldsymbol{k},\boldsymbol{q}\,|\,\Delta_\beta)\,\frac{f_0(\varepsilon^\gamma_\beta(k)) - f_0(\varepsilon^{\gamma'}_\beta(|\boldsymbol{k}+\boldsymbol{q}|))}{\hbar\omega + i0^+ + \varepsilon^\gamma_\beta(k) - \varepsilon^{\gamma'}_\beta(|\boldsymbol{k}+\boldsymbol{q}|)}\,, \qquad (7)$$

where the electron transitions between different spins or valleys are excluded, $f_0(x) = \{1 + \exp[(x - \mu_T)/k_BT]\}^{-1}$ is the Fermi functions for thermal-equilibrium electrons and holes, and it reduce to Heaviside function $\Theta\left(E_F - \varepsilon_\beta^\gamma(k)\right)$ at $T = 0$. Meanwhile, the prefactor $\mathcal{F}_{\gamma,\gamma'}(\boldsymbol{k}, \boldsymbol{q} \,|\, \Delta_\beta)$ in Eq. (7) represents an overlap of the electron ($\gamma = +1$) and hole ($\gamma = -1$) wavefunctions of the same subband (fixed β for the same spin and valley) at two different wavevectors $\boldsymbol{k}$ and $\boldsymbol{k} + \boldsymbol{q}$, i.e.,

$$2\,\mathcal{F}_{\gamma,\gamma'}(\boldsymbol{k}, \boldsymbol{q} \,|\, \Delta_\beta) = 1 + \gamma\gamma' \,\frac{(\hbar v_F)^2\, \boldsymbol{k} \cdot (\boldsymbol{k} + \boldsymbol{q}) + \Delta_\beta^2}{\left|\varepsilon_\beta^\gamma(k)\, \varepsilon_\beta^\gamma(|\boldsymbol{k} + \boldsymbol{q}|)\right|} \ . \tag{8}$$

Here, no valley or spin change under optical excitations is allowed so that only one index β occurs in Eq. (6), different from the summation over electron/hole indexes γ and γ' in Eq. (7) for pseudo spins.

For easiness in computation, instead of using Eq. (7) directly, we utilize a thermal-convolution technique [62] for $T > 0$ from the zero-T polarization function $\Pi^{(0)}(q, \omega \,|\, E_F, \Delta_\beta)$.

Compared to Eq. (7), this approach has an advantage of dealing with a known analytic expression [25,59,60,63] for $\Pi^{(0)}(q, \omega \,|\, E_F, \Delta_\beta)$. This thermal convolution will be done for all accessible frequencies ω and wavenumbers q, including the static and long-wavelength limits.

The imaginary part of $\Pi_T(q, \omega \,|\, \mu_T, \Delta_\beta)$ (associated with Landau damping) as functions of ω and T for various n_c (related to E_F) and T are presented in Fig. 2. The plasmon Landau damping has a resonance for fixed $q = 0.8\, k_0$ in (a), which becomes more significant with increasing T. In comparison with (a), a high-frequency should-like feature develops as $q = 1.5\, k_0$ in (b). As doping density n_c (or E_F) is increased in (c) with $q = 1.5\, k_0$ and $k_BT/E_0 = 0.1$, the resonance in Landau damping is greatly enhanced and shifted to higher frequencies. However, for non-resonant Landau damping as a function of k_BT in (d) with $E_F/E_0 = 1.0$ and $q = 1.4\, k_0$, its reduction with T becomes less and less significant with increasing ω.

On the other hand, the real part of $\Pi_T(q, \omega \,|\, \mu_T, \Delta_\beta)$ as functions of ω and q for different fixed q and ω values are presented in Fig. 3. At $k_BT/E_0 = 0.05$, we find from (a) that the plasmon energy is pushed up by increase of q. This enhancement of plasmon energy with q (or the group velocity) becomes larger at a relatively high temperature $k_BT/E_0 = 0.5$ in (b).

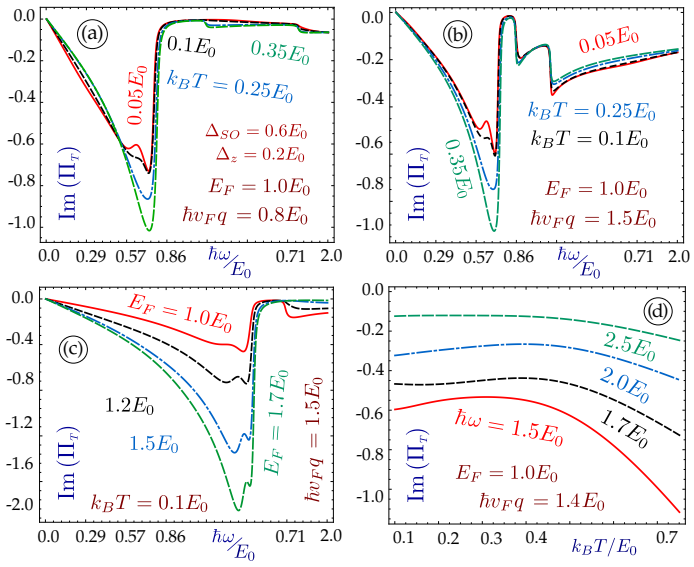

FIG. 2: (Color online) $\mathrm{Im}[\Pi_T(q,\omega\,|\,\mu_T,\Delta_\beta)]$ (in units of k_0^2/E_0) for silicene with $\Delta_{SO}/E_0 = 0.6$, $\Delta_z/E_0 = 0.2$ and various values of n_c. Panels (a)-(c) present $\hbar\omega$ dependence for $q = 0.8\,k_0$ (a), $1.5\,k_0$ (b) and (c). Different curves in (a) and (b) are associated with $E_F/E_0 = 1$, and $k_BT/E_0 = 0.05$ (red solid), 0.1 (black dashed), 0.25 (blue dash-dotted), 0.35 (green dashed). Panel (c) presents similar results for $k_BT/E_0 = 0.1$, and $E_F/E_0 = 1$ (red solid), 1.2 (black short-dashed), 1.5 (blue dash-dotted), 1.7 (green dashed). Plot (d) shows k_BT dependence with $E_F/E_0 = 1$, $q = 1.4\,k_0$, and $\hbar\omega/E_0 = 1.5$ (red solid), 1.7 (black short-dash), 2 (blue dash-dotted), 2.5 (green dashed) for various curves.

Similar increases of plasmon wavenumber can also be seen from (c) and (d) as the frequency ω goes up at both low and intermediate T, respectively.

IV. CONDUCTIVITIES

We now further proceed to conductivities for doped silicene by using the obtained T and E_F dependent optical-polarization function in Sec. III. We will mainly focus on optical conductivity, which is related to polarization function in the long-wavelength limit, as well as the transport conductivity, which is calculated based on semiclassical Boltzmann theory including polarization function in the static limit.

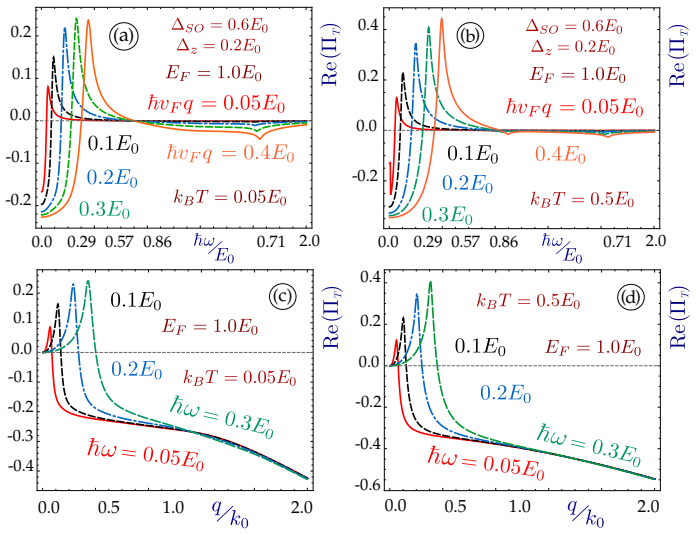

FIG. 3: (Color online) $\mathrm{Re}[\Pi_T(q,\omega\,|\,\mu_T,\Delta_\beta)]$ (in units of k_0^2/E_0) for silicene with $\Delta_{SO}/E_0 = 0.6$, $\Delta_z/E_0 = 0.2$ and $E_F/E_0 = 1$. Panels (a) and (b) show $\hbar\omega$ dependence for various curves with $q/k_0 = 0.05$ (red solid), 0.1 (black short-dashed), 0.2 (blue dash-dotted), 0.3 (green dashed), 0.4 (orange solid). Plots (c) and (d) demonstrate q dependence of curves with relatively small $\hbar\omega/E_0 = 0.05$ (red solid), 0.1 (black short-dashed), 0.2 (blue dash-dotted), 0.3 (green dashed). In addition, $k_BT/E_0 = 0.05$ in (a) and (c) while $k_BT/E_0 = 0.5$ in (b) and (d).

A. Optical Conductivity

The optical conductivity, which connects the polarization-current density (per atomic-layer thickness) to the incident electromagnetic field with various frequencies due to light-induced density fluctuations (mostly direct interband optical transitions of electrons), is often used in characterizing material optical properties, e.g., absorptions, transmissions and reflections. For graphene, these optical properties were examined in both visible and infrared frequency ranges. In the former case, graphene transmittance was predicted [64–66] to be independent of light frequency ω, and it was confirmed [67] by directly measuring the optical conductivity, reflectivity and transmission for photon energies exceeding 200 meV. The calculations of graphene optical conductivity in the visible range using the next-nearest-neighbor tight-binding model justified the Dirac-cone approximations well above normally accepted energy range. Applying the Dirac-cone approximation, we have shown [68] that the induced optical polarization in graphene affects the hybridization of radiative and evanescent electromagnetic fields, which results in localized polarization fields along with a modifica-

tion of an incident surface plasmon-polariton field. Studies of Dirac quasiparticle transport in graphene under a magnetic field, e.g., Hall and optical conductivities, were reported in Ref. [69]. Additionally, a generalized model for the nonlinear optical conductivity of generic two band systems (gapped or gapless graphene) demonstrated that such nonlinearities can be controlled by a single dimensionless parameter proportional to the incident-field strength. [70]

The general relation between the optical conductivity and optical-polarization function was discussed by us before [52]. In the long-wavelength limit ($q \to 0$), an incident electromagnetic field can be treated as a spatially-uniform one. In the following, we present a detailed study on the dependence of optical conductivity on T, E_F and Δ_β in silicene. Under the long-wavelength limit, the optical conductivity for a weak incident light is simply related to the dynamical polarization function through [71,72]

$$\sigma_O^{(T)}(\omega \,|\, \mu_T, \Delta_\beta) = i\omega\, e^2 \lim_{q\to 0} \frac{\Pi_T(q, \omega \,|\, \mu_T, \Delta_\beta)}{q^2} \ . \tag{9}$$

Here, it is important to point out that $\Pi_T(q, \omega \,|\, \mu_T, \Delta_\beta) \backsim q^2$ as $q \to 0$ for all 2D systems, regardless of the bandgaps [60] and temperatures [55,58,73]. Therefore, the optical conductivity in Eq. (9) becomes independent of q. Meanwhile, such a limiting behavior in $\Pi_T(q, \omega \,|\, \mu_T, \Delta_\beta)$ also contributes a $\backsim \sqrt{q}$ dependence to the plasmon dispersion relation.

By starting the case with $T = 0$, the polarization function for $q \to 0$ is given explicitly by [59,60,73]

$$\begin{aligned}
\mathrm{Re}\left[\Pi^{(0)}(q, \omega \,|\, E_F, \Delta_\beta)\right] &= \frac{q^2}{4\pi\hbar\omega} \sum_{\beta=\pm 1} \left\{ \frac{4E_F}{\hbar\omega} \left[1 - \left(\frac{\Delta_\beta}{E_F}\right)^2\right] \right. \\
&+ \left. \left[1 + \left(\frac{2\Delta_\beta}{\hbar\omega}\right)^2\right] \ln\left|\frac{2E_F - \hbar\omega}{2E_F + \hbar\omega}\right| \right\} \ , \\
\mathrm{Im}\left[\Pi^{(0)}(q, \omega \,|\, E_F, \Delta_\beta)\right] &= -\frac{q^2}{4\hbar\omega}\, \Theta\left(\hbar\omega - 2E_F\right) \sum_{\beta=\pm 1} \left[1 + \left(\frac{2\Delta_\beta}{\hbar\omega}\right)^2\right] \ ,
\end{aligned} \tag{10}$$

where the logarithm term in $\mathrm{Re}[\Pi^{(0)}(q, \omega \,|\, E_F, \Delta_\beta)]$ has a negligible contribution to the undamped plasmon dispersion relation for $\hbar\omega \ll E_F$ and it is often neglected in previous studies. Equation (10) leads to the so-called *absorption threshold* [64–66] defined as $\omega_0 \backsim 2E_F/\hbar$ under which $\mathrm{Im}\left[\Pi^{(0)}(q, \omega \,|\, E_F, \Delta_\beta)\right] = 0$, and it is independent of Δ_β. However, this logarithm

term can still significantly affect $\mathrm{Re}\left[\Pi^{(0)}(q,\omega\,|\,E_F,\Delta_\beta)\right]$ above this absorption threshold.

From Eq. (9) we know that the real (imaginary) part of $\sigma_O^{(T)}(\omega\,|\,\mu_T,\Delta_\beta)$ is related to the imaginary (real) part of $\Pi_T(q,\omega\,|\,\mu_T,\Delta_\beta)$, respectively. Using Eq. (10) we find for $T=0$

$$\begin{aligned}
\mathrm{Im}\left[\sigma_O^{(0)}(\omega\,|\,E_F,\Delta_\beta)\right] &= \frac{e^2}{4\pi\hbar}\sum_{\beta=\pm1}\left\{\frac{4E_F}{\hbar\omega}\left[1-\left(\frac{\Delta_\beta}{E_F}\right)^2\right]\right. \\
&+ \left.\left[1+\left(\frac{2\Delta_\beta}{\hbar\omega}\right)^2\right]\ln\left|\frac{2E_F-\hbar\omega}{2E_F+\hbar\omega}\right|\right\}\,, \\
\mathrm{Re}\left[\sigma_O^{(0)}(\omega\,|\,E_F,\Delta_\beta)\right] &= \frac{e^2}{4\hbar}\,\Theta\left(\hbar\omega-2E_F\right)\sum_{\beta=\pm1}\left[1+\left(\frac{2\Delta_\beta}{\hbar\omega}\right)^2\right]\,, \qquad (11)
\end{aligned}$$

where $\mathrm{Re}\left[\sigma_O^{(0)}(\omega\,|\,E_F,\Delta_\beta)\right]=0$ as long as $\hbar\omega<2E_F$, which is referred to as a *state-blocking effect* [67,69,70] due to Pauli exclusions and is attributed to the step-like distribution function at $T=0$ in Eq. (7). At finite T, however, the step-like distribution function in Eq. (7) can still be approximated by [64,74]

$$\Theta\left(E_F-\varepsilon_\beta^\gamma(k)\right)\Longrightarrow\frac{1}{2}\left\{1-\tanh\left[\frac{\varepsilon_\beta^\gamma(k)-\mu_T}{2k_BT}\right]\right\}\,. \qquad (12)$$

Consequently, the ω dependence in $\mathrm{Re}\left[\sigma_O^{(T)}(\omega\,|\,\mu_T,\Delta_\beta)\right]$ will be smooth and nonzero. Furthermore, we know from Eqs. (10) and (12) that $\mathrm{Im}\left[\Pi_T(q,\omega\,|\,\mu_T,\Delta_\beta)\right]$ is nonzero at finite T with a thermal tail. This leads to a nonzero $\mathrm{Re}\left[\sigma_O^{(T)}(\omega\,|\,\mu_T,\Delta_\beta)\right]$ as a function of ω. We further expect that $\mathrm{Re}\left[\sigma_O^{(T)}(\omega\,|\,\mu_T,\Delta_\beta)\right]$ will depend on T substantially since $\mathrm{Im}\left[\Pi_T(q,\omega\,|\,\mu_T,\Delta_\beta)\right]$ decreases as $1/T$ in the high-T limit for all q values.

Making use of the results in Ref. [58], for gapless ($\Delta_\beta=0$) but doped ($E_F>0$) graphene we obtain a simple result for optical conductivity in the high-T limit ($k_BT\gg E_F$ and $\hbar\omega$)

$$\begin{aligned}
\sigma_O^{(T)}(\omega\,|\,\mu_T,\Delta_\beta=0) \backsimeq \frac{e^2}{\hbar}&\left\{\frac{\hbar\omega}{16k_BT}\left[1-\frac{1}{3}\left(\frac{\hbar\omega}{4k_BT}\right)^2\right]\right. \\
&\left.+i\,\frac{2\ln 2\,k_BT}{\pi\hbar\omega}\left[1+2\ln 2\left(\frac{E_F}{4\ln 2\,k_BT}\right)^4\right]\right\}\,, \qquad (13)
\end{aligned}$$

where we have already employed the relation [58] $\mu_T\approx(E_F^2/4\ln 2\,k_BT)$ for high T. It is evident from Eq. (13) that $\mathrm{Im}\left[\sigma_O^{(T)}(\omega\,|\,\mu_T,\Delta_\beta=0)\right]$ is large but only weakly depend on E_F.

Meanwhile, $\mathrm{Re}\left[\sigma_O^{(T)}(\omega\,|\,\mu_T,\Delta_\beta=0)\right]$ is small and decreases as $1/T$ within this high-T limit.

On the other hand, for gapped ($\Delta_\beta=\Delta_0$) but undoped ($E_F=0$) graphene at high T ($k_BT\gg\Delta_0$ and $\hbar\omega$), we find the optical conductivity

$$\mathrm{Re}\left[\sigma_O^{(T)}(\omega\,|\,\mu_T,\Delta_0)\right]_{E_F=0}=\frac{e^2}{16\hbar}\left(\frac{\hbar\omega}{k_BT}\right)\left(1-\frac{\Delta_0}{\hbar\omega}\right)\ ,$$
$$\mathrm{Im}\left[\sigma_O^{(T)}(\omega\,|\,\mu_T,\Delta_0)\right]_{E_F=0}=\frac{4e^2}{\pi\hbar}\left(\frac{k_BT}{\hbar\omega}\right)\left\{2\ln 2-\left(\frac{\Delta_0}{k_BT}\right)^2\left[\mathbb{C}_0-\ln\left(\frac{\Delta_0}{2k_BT}\right)\right]\right\}\ , \quad (14)$$

where $\mathbb{C}_0\backsimeq 0.79$ is a constant. It is interesting to note from Eq. (14) that the real and imaginary parts of $\sigma_O^{(T)}(\omega\,|\,\mu_T,\Delta_0)$ for $E_F=0$ acquire an inverse dependence on $\hbar\omega/k_BT$. Again, $\mathrm{Im}\left[\sigma_O^{(T)}(\omega\,|\,\mu_T,\Delta_0)\right]$ only weakly depends on Δ_0. If T is really high, the thermal population of the upper Dirac cone cannot be ignored even for $E_F=0$. In this case, the factor $k_BT/\hbar\omega$ in Eq. (14) plays a similar role of $E_F/\hbar\omega$ in Eq. (11) for the imaginary part of the optical conductivity at $T=0$.

Finally, for silicene with two inequivalent bandgaps $\Delta_\beta=\Delta_{>,<}$, the corresponding result is a summation over these two bandgaps, yielding

$$\sigma_O^{(T)}(\omega\,|\,\mu_T)=\sum_{\beta=\pm1}\sigma_O^{(T)}(\omega\,|\,\mu_T,\Delta_\beta)\ . \quad (15)$$

Here, no analytical results for optical conductivity at intermediate T can be obtained. For this situation, we present our numerical results in Figs. 4 and 5.

The real and imaginary parts of $\Pi_T(q,\omega\,|\,\mu_T)$ are connected by the Kramers-Kronig relations, implying similar connections between the real and imaginary parts of $\sigma_O^{(T)}(\omega\,|\,\mu_T)$. Specifically, the discontinuities in $\mathrm{Re}\left[\sigma_O^{(T)}(\omega\,|\,\mu_T)\right]$ can be related to the negative peaks in $\mathrm{Im}\left[\sigma_O^{(T)}(\omega\,|\,\mu_T)\right]$, as shown in Figs. 4($a$) and 4($b$) for $T=0$. Moreover, the peak positions depend on T, as seen from Figs. 4(b) and 4(d), mainly due to a nontrivial T dependence of μ_T (see the labels for calculated μ_T in Figs. 4 and 5). In fact, the steps or peaks at $T=0$ are found exactly at the absorption threshold $\hbar\omega=2E_F$. For high T, however, the absorption threshold for graphene is approximated by [64,66] $(\hbar\omega-2E_F)^2\Longrightarrow(\hbar\omega-2\mu_T)^2+(2k_BT)^2$, where μ_T decreases with T. Consequently, the peak positions will not simply follow $\hbar\omega=2\mu_T$ at finite T.

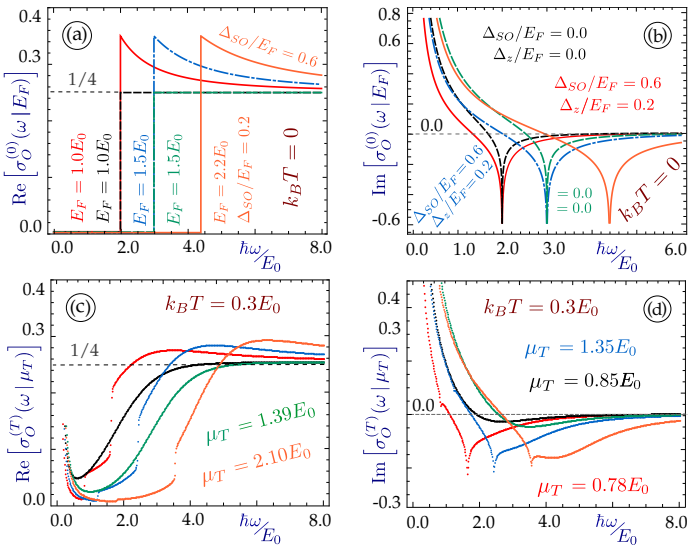

FIG. 4: (Color online) $\sigma_O^{(T)}(\omega\,|\,\mu_T)$ (in units of $e^2/\hbar$) of silicene from Eq. (15) in low-T regime. Panels (a), (c) show its real part as function of $\hbar\omega$, while panels (b), (d) give its imaginary part. Here, we take $T = 0$ for (a), (b) but $k_BT/E_0 = 0.3$ in (c), (d). Different curves correspond to: $\Delta_{SO}/E_0 = 0.6$, $\Delta_z/E_0 = 0.2$, $E_F/E_0 = 1$ (red); $\Delta_{SO} = \Delta_z = 0$, $E_F/E_0 = 1$ (black); $\Delta_{SO}/E_0 = 0.9$, $\Delta_z/E_0 = 0.3$, $E_F/E_0 = 1.5$ (blue); $\Delta_{SO} = \Delta_z = 0$, $E_F/E_0 = 1.5$ (green); $\Delta_{SO}/E_0 = 1.32$, $\Delta_z/E_0 = 0.44$, $E_F/E_0 = 2.2$ (orange).

As seen from Fig. 4, the ω dependence in $\sigma_O^{(T)}(\omega\,|\,\mu_T)$ at low T is similar to the case of $T = 0$, where $\sigma_O^{(0)}(\omega\,|\,E_F)$ can be analytically calculated based on the derived expressions for $\Pi^{(0)}(q,\omega\,|\,E_F)$ in Ref. [25]. At $k_BT/E_0 = 0.3$, our systems with zero bandgaps show no negative peaks in $\mathrm{Im}\left[\sigma_O^{(T)}(\omega\,|\,\mu_T)\right]$, and $\mathrm{Re}\left[\sigma_O^{(T)}(\omega\,|\,\mu_T)\right]$ only displays a smooth and monotonic increase (no discontinuities) with ω up to 1/4. For intermediate T, as exhibited in Fig. 5, two steps (rising above 1/4) and double peaks appear clearly in $\mathrm{Re}\left[\sigma_O^{(T)}(\omega\,|\,\mu_T)\right]$ and $\mathrm{Im}\left[\sigma_O^{(T)}(\omega\,|\,\mu_T)\right]$, respectively, due to the presence of two different continua for interband particle-hole modes (from different bandgaps $\Delta_<$, $\Delta_>$). Even for $k_BT/E_0 = 1$, two negative peaks and jumps are still visible in Figs. 5(c) and 5(d).

B. Transport Conductivity

We now turn to calculating the transport conductivity in doped silicene and gapped graphene in the presence of an elastic scattering of electrons by ionized impurities screened

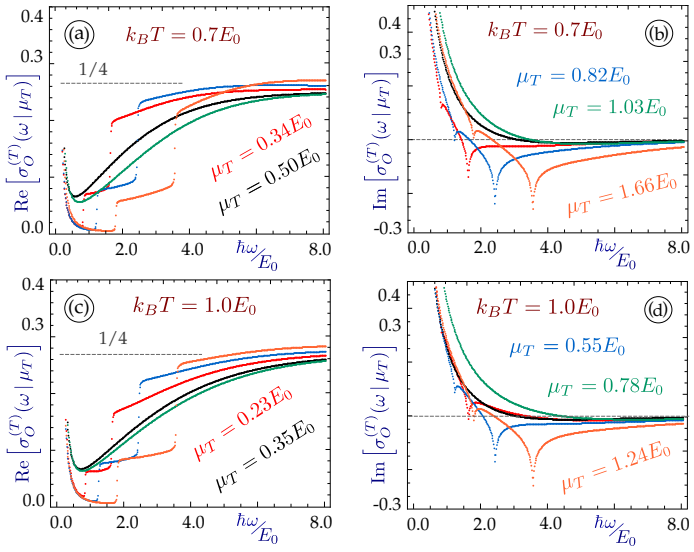

FIG. 5: (Color online) $\sigma_O^{(T)}(\omega\,|\,\mu_T)$ (in units of $e^2/\hbar$) of silicene at intermediate T. Panels (a), (c) display its real part as function of $\hbar\omega$, while panels (b), (d) present its imaginary part. Here, we choose $k_BT/E_0 = 0.7$ for (a), (b) while $k_BT/E_0 = 1$ in (c), (d). Various curves are related to: $\Delta_{SO}/E_0 = 0.6$, $\Delta_z/E_0 = 0.2$, $E_F/E_0 = 1$ (red); $\Delta_{SO} = \Delta_z = 0$, $E_F/E_0 = 1$ (black); $\Delta_{SO}/E_0 = 0.9$, $\Delta_z/E_0 = 0.3$, $E_F/E_0 = 1.5$ (blue); $\Delta_{SO} = \Delta_z = 0$, $E_F/E_0 = 1.5$ (green); $\Delta_{SO}/E_0 = 1.32$, $\Delta_z/E_0 = 0.44$, $E_F/E_0 = 2.2$ (orange).

by a temperature-dependent dielectric function $\epsilon_T(q)$ determined from Eq. (5) under the static limit $\omega \to 0$. Based on the Boltzmann transport equation, effects of elastic, inelastic and electron-pair scatterings were extensively studied by us in semiconductors [41–43] and graphene [53] beyond the relaxation-time approximation [75] for a strong bias field. For a weak bias field, the Boltzmann theory was used in Ref. [57] for the transport conductivity of gapless graphene, showing a non-monotonic temperature dependence. In the presence of bandgaps, however, the nontrivial T dependence in μ_T must be taken into account, as discussed in Sec. II.

When the external bias voltage is very low in comparison with E_F, the general Boltzmann transport equation can be simplified by the relaxation-time approximation for particle collisions. Consequently, we obtain the transport conductivity for $\gamma = \gamma' = +1$ from

$$\sigma_B^{(T)}(\mu_T|\Delta_0) = \frac{e^2 v_F^2}{2} \int_{\Delta_0}^{\infty} d\varepsilon \left[-\frac{\partial f_0(\varepsilon)}{\partial \varepsilon}\right] \rho_d(\varepsilon) \tau_e^{(T)}(\varepsilon) \left(1 - \frac{\Delta_0^2}{\varepsilon^2}\right) , \tag{16}$$

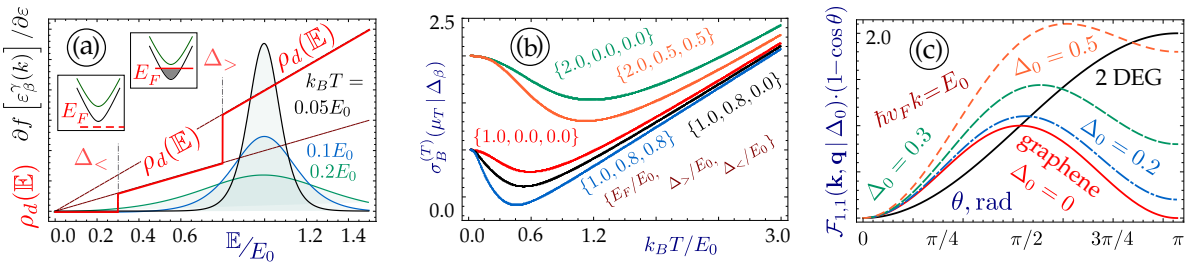

FIG. 6: (Color online) Panel (a) shows the overlay of the two-step DoS $\rho_d(\mathbb{E})$ (in units of k_0^2/E_0) of silicene with $\partial f_0(\mathbb{E})/\partial\mathbb{E}$ (in units of E_0^{-1}) as functions of energy $\mathbb{E}$ at various T. Plot (b) presents the transport conductivity $\sigma_B^{(T)}(\mu_T|\Delta_\beta)$ (in units of $e^2/\hbar$) as functions of k_BT for different combinations of E_F/E_0, $\Delta_</E_0$ and $\Delta_>/E_0$. Plot (c) displays the dimensionless factor $\mathcal{F}_{1,1}(\mathbf{k},\mathbf{q}|\Delta_0)\,(1-\cos\theta)$ as functions of scattering angle θ with fixed $k=k_0$ and different values of Δ_0, where $|\mathbf{q}|=2k\sin(\theta/2)$ and the result for 2DEG is also shown for a comparison.

where $\rho_d(\varepsilon)$ is the DoS only for $\gamma=+1$, $\tau_e^{(T)}(\varepsilon)$ is the energy-relaxation time for driven carriers, and the factor $(1-\Delta_0^2/\varepsilon^2)$ represents the reduction of group velocity by a bandgap. For electron doping with $E_F>0$ in gapped graphene, the integration in Eq. (16) is only carried out over the conduction band energies. At $T=0$, we have $[-\partial f_0(\varepsilon)/\partial\varepsilon]\Longrightarrow\delta(\varepsilon-E_F)$ and $E_F>\Delta_0$. For low temperatures $k_BT\ll E_F$, $[-\partial f_0(\varepsilon)/\partial\varepsilon]$ can still be approximated by $\delta(\varepsilon-E_F)$, and therefore only electrons around the Fermi energy E_F will contribute to conduction. For high temperatures $k_BT\gg E_F$, on the other hand, $[-\partial f_0(\varepsilon)/\partial\varepsilon]$ becomes nonzero for all energies outside the bandgap region $\varepsilon>\Delta_0$. This situation is illustrated in Fig. 6(a) for silicene with two inequivalent bandgaps $\Delta_\beta=\Delta_>$ or $\Delta_<$. Consequently, we expect that a large Δ_β value always reduces conductivities due to a smaller group velocity and a reduced DoS for contributions of low-energy electrons at high T, as seen from Fig. 6(b).

An important quantity in our conductivity calculation is the energy-relaxation time $\tau_e^{(T)}(\varepsilon|\Delta_\beta)$ calculated by the second-order Born approximation [57,76,77] for $\gamma=+1$ as

$$\frac{1}{\tau_e^{(T)}(\varepsilon|\Delta_\beta)}=\frac{2\pi N_i}{\hbar}\int\frac{d^2\mathbf{k}'}{(2\pi)^2}\left|\frac{v(|\mathbf{k}'-\mathbf{k}|)}{\epsilon_T(|\mathbf{k}'-\mathbf{k}|)}\right|^2$$
$$\times\delta\left(\varepsilon_\beta^\gamma(k)-\varepsilon_\beta^\gamma(k')\right)\,\mathcal{F}_{\gamma,\gamma}(\mathbf{k},\mathbf{k}'-\mathbf{k}\,|\,\Delta_\beta)\,(1-\cos\theta_{\mathbf{k},\mathbf{k}'})\ , \tag{17}$$

where N_i represents the impurity areal density, the inter-valley impurity scattering is ignored

due to very large momentum transfer, the energy-conservation constraint for elastic impurity scattering is employed, i.e., $\gamma = \gamma' = 1$, $\theta_{\mathbf{k},\mathbf{k}'}$ is the elastic scattering angle [75], and $\epsilon_T(q) \equiv \epsilon_T(q, \omega = 0)$ given by Eq. (5). The overlap factor $\mathcal{F}_{\gamma,\gamma'}(\mathbf{k}, \mathbf{q}|\Delta_\beta)$ is determined from Eq. (21), and the angular dependence of the factor $\mathcal{F}_{1,1}(\mathbf{k}, \mathbf{q}|\Delta_0)\,(1 - \cos\theta)$ in Eq. (17) for $k = k_0$ and different values of Δ_0 is displayed in Fig. 6(c), from which we find that the results for two-dimensional electron gas (2DEG) and gapless monolayer graphene are quite different. The full-back scattering ($\theta = \pi$) becomes very strong for 2DEG but vanishes for gapless graphene. A finite Δ_0 value lifts the full-back scattering from zero in gapped graphene. The increase of Δ_0 enhances the peak strength, pushes the peak θ value towards a larger one and gradually enhances the scattering rate in Eq. (17). As a result, the energy-relaxation time $\tau_e^{(T)}(\varepsilon)$ in Eq. (16) decreases with Δ_0, which provides an additional mechanism for a decreasing transport conductivity besides the reduced group velocity and DoS.

If graphene is subjected to an irradiation of circularly-polarized light, [78] the opened energy gap is found also leading to a monotonic decrease of the transport conductivity [79] by the ratio $\backsimeq (E_F^2 - \Delta_0^2)/(E_F^2 + 3\Delta_0^2)$, which is attributed to the decrease of the Fermi velocity from v_F for gapless graphene to $v_F[1 - (\Delta_0/E_F)^2]^{1/2}$ in the presence of a bandgap Δ_0.

Equation (17) could be further simplified due to the presence of delta function for energy conservation in elastic scattering. Let us first consider gapped graphene with fourfold-degenerate energy subbands and a single, finite gap Δ_0. One way is to perform the radial integration first with respect to $\mathbf{k}'$ by using the delta function, which leads to

$$\frac{1}{\tau_e^{(T)}(\varepsilon|\Delta_0)} \frac{2N_i}{\pi\hbar} \frac{\sqrt{\varepsilon_k^2 - \Delta_0^2}}{(\hbar v_F)^2} \int_0^1 d\xi \, \frac{\xi^2}{\sqrt{1-\xi^2}}$$
$$\times \left\{1 + \frac{\Delta_0^2 + (1-2\xi^2)(\varepsilon_k^2 - \Delta_0^2)}{\varepsilon_k^2}\right\} \left(\frac{k\xi}{\alpha\pi} - \Pi_T(2\xi k, \omega = 0\,|\,\mu_T, \Delta_0)\right)^{-2} , \qquad (18)$$

where $\varepsilon \equiv \varepsilon_k = \sqrt{(\hbar v_F k)^2 + \Delta_0^2} \geq \Delta_0$, and the expression in Eq. (21) for $\mathcal{F}_{1,1}(\mathbf{k}, \mathbf{k}' - \mathbf{k}|\Delta_0)$ has been employed. Alternatively, we can also calculate first the angular θ integration with respect to $\mathbf{k}'$ under the condition $|\mathbf{k}| = |\mathbf{k}'|$, yielding

$$\frac{1}{\tau_e^{(T)}(\varepsilon|\Delta_0)} = \frac{N_i}{\pi\hbar}\frac{\varepsilon}{(\hbar v_F)^2}\int_0^{2k}\frac{dq}{k}\left(\frac{q}{k}\right)^2\left[1-\left(\frac{q}{2k}\right)^2\right]^{-1/2} \times \left[1+\frac{\Delta_0^2+(\hbar v_F k)^2\,(1-2q^2/k^2)}{\Delta_0^2+(\hbar v_F k)^2}\right]\left[\frac{q}{2\pi\alpha}-\Pi_T(q,\omega=0|\mu_T,\Delta_0)\right]^{-2}\ , \quad (19)$$

where $q=2k\sin(\theta/2)$ and $k=\sqrt{\varepsilon^2-\Delta_0^2}/(\hbar v_F)$.

Silicene has two inequivalent bandgaps $\Delta_{<,>}$, and we need to calculate the wavefunction overlaps between these two different bandgaps as a generalization of the result in Eq. (8). For this case, the pseudo-spin wavefunction is written as

$$\Psi_\beta^\gamma(k\,|\,\Delta_\beta)=\frac{1}{\sqrt{2\,\mathbb{E}_\beta(k)}}\begin{bmatrix}\sqrt{\mathbb{E}_\beta(k)+\gamma\Delta_\beta}\\ \gamma\sqrt{\mathbb{E}_\beta(k)-\gamma\Delta_\beta}\ \mathsf{e}^{i\Phi_{\mathbf{k}}}\end{bmatrix}\ , \quad (20)$$

where $\Phi_{\mathbf{k}}=\tan^{-1}(k_y/k_x)$, and $\mathbb{E}_\beta(k)=\varepsilon_\beta^\gamma(k)/\gamma=\sqrt{(\hbar v_F k)^2+\Delta_\beta^2}=\left|\varepsilon_\beta^\gamma(k)\right|$. Therefore, it is straightforward to calculate the overlap from

$$\begin{aligned}\mathcal{F}_{\gamma,\gamma'}(\boldsymbol{k},\boldsymbol{q}\,|\,\Delta_{1,2}) &= \left|\langle\Psi_1^\gamma(k\,|\,\Delta_1)\,|\,\Psi_2^{\gamma'}(|\boldsymbol{k}+\boldsymbol{q}|\,|\,\Delta_2)\rangle\right|^2\\ &= \frac{1}{2}\left\{1+\gamma\gamma'\,\frac{\Delta_1\Delta_2+(\hbar v_F)^2\,k\,|\boldsymbol{k}+\boldsymbol{q}|\cos\theta_{\mathbf{k},\mathbf{k}+\mathbf{q}}}{\mathbb{E}_1(k)\,\mathbb{E}_2(|\boldsymbol{k}+\boldsymbol{q}|)}\right\}\ , \end{aligned} \quad (21)$$

which reduces to Eq. (8) after taking $\Delta_1=\Delta_2$ and $\mathbb{E}_1=\mathbb{E}_2$. Here, we can apply a geometrical relation, i.e., $|\boldsymbol{k}+\boldsymbol{q}|\cos\theta_{\mathbf{k},\mathbf{k}+\mathbf{q}}=k+q\cos\phi$ (see Fig. 7), so as to express the final result of Eq. (17) by an integration variable $\xi=-\cos\phi$, yielding

$$\frac{1}{\tau_e^{(T)}(\varepsilon\,|\,\Delta_\beta)}=\frac{1}{4}\sum_{i,j=1,2}\frac{1}{\tau_e^{(T)}\,(\varepsilon\,|\,\Delta_1,\Delta_2)}\ , \quad (22)$$

which includes electron transitions between a pair of states with either the same or different bandgaps: $\mathbb{E}_i\Longrightarrow\mathbb{E}_i$, $\mathbb{E}_i\Longrightarrow\mathbb{E}_j$, $\mathbb{E}_j\Longrightarrow\mathbb{E}_i$ and $\mathbb{E}_j\Longrightarrow\mathbb{E}_j$. For a gapped graphene, we have $\Delta_1=\Delta_2=\Delta_0$ for all four terms in Eq. (22) and arrive at Eq. (18).

For two nondegenerate subbands in general, the allowed angle ϕ is determined by the following equation for the silicene lattice

$$\cos\phi=\frac{\Delta_i^2-\Delta_j^2}{2\,(\hbar v_F)^2kq}-\frac{q}{2k}\ , \quad (23)$$

where each $\Delta_{i,j}$ could take either $\Delta_>$ or $\Delta_<$, i.e., three different ϕ values are possible for given k and q. If two bandgaps become the same, there exists only one value from $\cos\phi = -q/2k$, as shown in Fig. 7.

For silicene at $T = 0$, the polarization function with two different bandgaps $\Delta_\beta = \Delta_{<,>} = |\Delta_{SO} + \beta\Delta_z|$ is given by [25,60]

$$\Pi^{(0)}(q, \omega = 0 \,|\, E_F, \Delta_\beta) = -\frac{E_F}{\pi} \sum_{\beta=\pm 1} f_<(q)\, \Theta(\Delta_\beta - E_F) + f_>(q)\, \Theta(E_F - \Delta_\beta) \;, \tag{24}$$

where

$$\begin{aligned} f_<(q) &= \frac{\Delta_\beta}{2E_F} + \left(\frac{\hbar v_F q}{4E_F} - \frac{\Delta_\beta^2}{4\hbar v_F q\, E_F} \right) \arcsin\left(\sqrt{1 + \left(\frac{2\Delta_\beta}{\hbar v_F q} \right)^2} \right) \;, \\ f_>(q) &= 1 - \Theta\left(q - 2k_F^\beta \right) \left[\frac{1}{2} \sqrt{1 - \left(\frac{2k_F^\beta}{q} \right)^2} \right. \\ &- \left. \left(\frac{\hbar v_F q}{4E_F} - \frac{\Delta_\beta^2}{4\hbar v_F q\, E_F} \right) \arctan\left(\frac{\hbar v_F \sqrt{q^2 - 4\left(k_F^\beta \right)^2}}{2E_F} \right) \right] \;. \end{aligned} \tag{25}$$

Here, two inequivalent Fermi wavenumbers $k_F^\beta = \sqrt{E_F^2 - \Delta_\beta^2}/\hbar v_F$ depend on bandgaps Δ_β. For gapped graphene, this result is simplified by the substitution $\Delta_{<,>} = \Delta_0$.

Our numerical results for the energy-relaxation rate $1/\tau_e^{(T)}(\varepsilon \,|\, \Delta_\beta)$ and the transport conductivity $\sigma_B^{(T)}(\mu_T |\, \Delta_\beta)$ are presented in Fig. 8. $\sigma_B^{(T)}(\mu_T |\, \Delta_\beta)$ in Fig. 8 (c) is found to increase with T due to thermal occupations of high-energy states in the upper subband with a larger group velocity. On the other hand, as T increases, the enhanced screening to the impurity scattering will reduce the energy-relaxation rate, as exhibited in Fig. 8 (a) and (b). Moreover, the polarization function is expected to decrease with a bandgap at all temperatures, especially showing a $[1 - (\Delta_0/E_F)^2]$ dependence at $T = 0$ in the long-wavelength limit.

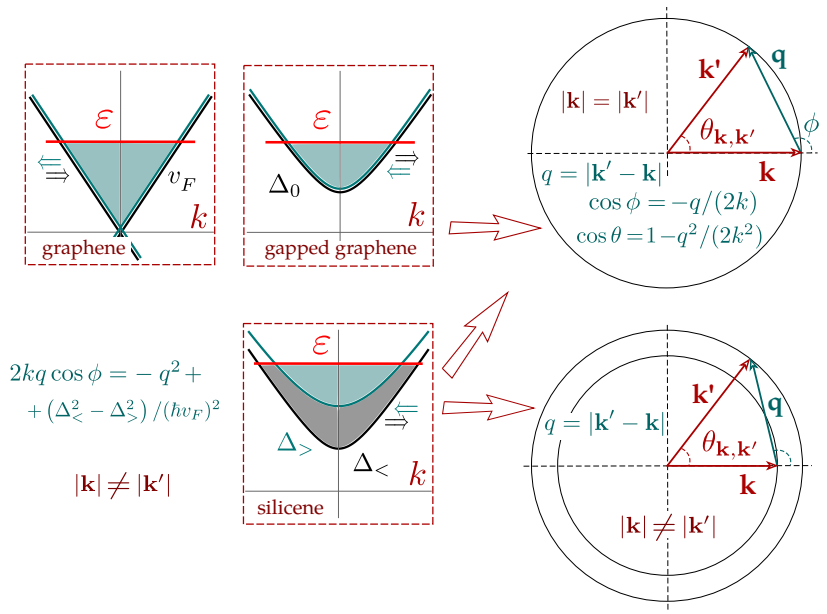

FIG. 7: (Color online) Schematics for wavevector relationships in an elastic scattering between $\varepsilon^{\gamma=1}_{\beta=\pm1}(k)$ and $\varepsilon^{\gamma=1}_{\beta=\pm1}(k')$ electron states with fourfold degeneracies $g_c = g_s g_v = 4$ in graphene and partially degenerate subbands in silicene lattice. For the latter, intersubband transitions with different magnitudes of wavevectors ($|\boldsymbol{k}| \neq |\boldsymbol{k}'|$) are allowed.

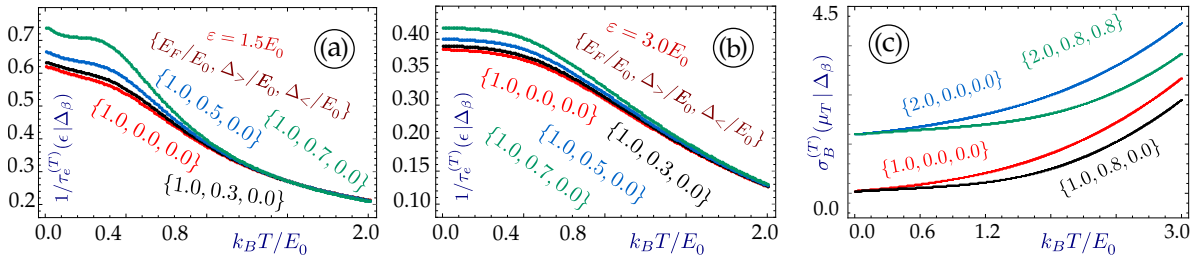

FIG. 8: (Color online) $1/\tau_e^{(T)}(\varepsilon|\,\Delta_B)$ (in units of $E_0/\hbar$) and $\sigma_B^{(T)}(\mu_T|\,\Delta_\beta)$ (in units of e^2/h) for silicene at various T. Plots (a) and (b) present the T dependence of $1/\tau_e^{(T)}(\varepsilon\,|\,\Delta_\beta)$ for $E_F/E_0 = 1.0$, $\Delta_> = \Delta_< = 0$ (red), $E_F = 1.0$, $\Delta_>/E_0 = 0.3$, $\Delta_< = 0$ (black), $E_F/E_0 = 1.0$, $\Delta_>/E_0 = 0.5$, $\Delta_< = 0$ (blue), and $E_F/E_0 = 1.0$, $\Delta_>/E_0 = 0.7$, $\Delta_< = 0$ (green). Panel (a) corresponds to $\varepsilon/E_0 = 1.5$, while plot (b) to $\varepsilon/E_0 = 3.0$. Panel (c) shows the T dependence of $\sigma_B^{(T)}(\mu_T|\,\Delta_\beta)$ for silicene with $E_F/E_0 = 1.0$, $\Delta_> = \Delta_< = 0$ (red), $E_F/E_0 = 1.0$, $\Delta_>/E_0 = 0.8$, $\Delta_< = 0$ (black), $E_F/E_0 = 2.0$, $\Delta_> = \Delta_< = 0.8$ (blue), and $E_F/E_0 = 2.0$, $\Delta_> = \Delta_< = 0$ (green).

V. CONCLUDING REMARKS

We have carried out calculations to investigate the optical and transport properties, i.e., the polarizability and transport current conductivity, for doped buckled honeycomb lattices with two inequivalent energy subbands. Emphasis has been placed on the effects of finite dopings and temperatures on the conductivities, i.e., by considering doped systems at arbitrary temperatures.

In our calculations, the dynamical polarization function is found to play a key role in studies of both optical and transport currents. For finite temperatures, the polarizability is computed either through a thermal-convolution approach starting with a zero-temperature one, or by a direct substitution of the Fermi functions. In either case, it is necessary to find out in advance a temperature-dependent chemical potential or a thermal path for a chosen system. Quite different from the two-dimensional electron gases, the calculated chemical potential decreases with temperature but never reaches zero for band structures with an electron/hole symmetry, such as silicene. In fact, the chemical potential increases monotonically with doping density (or Fermi energy) at all temperatures but becomes more significant at low densities or high temperatures. The unique temperature dependence found in a chemical potential due to thermal populations of an upper subband leads to specific thermal features in both the dynamical polarization function and static screening to electron-impurity interactions included in the Boltzmann transport equation. The interplay between electron doping and temperature in the real and imaginary parts of a dynamical polarization function is found nontrivial due to the existence of dual bandgaps. All of these new physical effects have been applied for the first time to the Boltzmann transport equation.

Starting with some known results for the polarizability in gapless graphene, we have derived analytic expressions for the optical conductivities for gapped graphene and silicene in both zero-temperature and high-temperature limits. At zero temperature, the existing negative peaks in $\mathrm{Im}[\sigma_O^{(T)}(\omega|\,\mu_T)]$ correspond to the absorption threshold at $\hbar\omega = 2E_F$, independent of bandgaps. Instead, the bandgaps do affect the non-rectangular shape of steps in $\mathrm{Re}[\sigma_O^{(T)}(\omega|\,\mu_T)]$. At finite temperatures, the sharp step is rounded off and the negative peaks shift to low frequencies. Physically, both steps and negative peaks originate from the intraband particle-hole modes in the $q \to 0$ limit, which depend on temperature but not through the chemical potential. Each peak has been calculated and identified. The

thermal shift of a negative peak ($\hbar\omega = 2E_F$ at $T = 0$) in the imaginary part of an optical conductivity does not follow the expected $\hbar\omega = 2\mu_T(E_F, T)$ temperature dependence and has been attributed to thermal variations in the boundaries of two separated continua with respect to different intersubband particle-hole modes under dual bandgaps. These unique spectral features can be applied to study plasmon damping in silicene and used for ultrafast light modulators based on field-tuned bandgaps.

Finally, we have also explored the transport conductivity $\sigma_B^{(T)}(\mu_T|\,\Delta_\beta)$ within the energy-relaxation-time approximation for gapped graphene and silicene. By extending the semi-analytic expressions for gapless-graphene inverse-relaxation time obtained in Ref. [57] to finite bandgaps, we have found a significant reduction in $\sigma_B^{(T)}(\mu_T|\,\Delta_\beta)$ at low temperatures. In the presence of two inequivalent subbands of silicene, we have observed that $\sigma_B^{(T)}(\mu_T|\,\Delta_\beta)$ increases with temperatures and doping densities due to enhanced group velocities at higher electron energies as well as due to enlarged screening to the impurity scattering at the same time. Contrary to previously considered graphene with or without energy bandgap, the inclusion of two new bandgaps in buckled honeycomb lattices gives rise to additional inter-subband elastic-scattering channels. As a result, more electron transitions can contribute to an energy-relaxation rate, which dramatically modifies the electron dynamics in Boltzmann transport.

In comparison with Kubo formula for band transports, the use of Boltzmann transport equation for doped buckled honeycomb lattices at finite temperatures has its own advantages in rigorously treating particle collisions. For elastic scattering of electrons with impurities, we have calculated explicitly the energy-dependent relaxation rate within the second-order Born approximation, instead of treating it as a phenomenological parameter as in Kubo's formula. These findings for transport conductivities are useful for investigating electron dynamics in innovative gapped Dirac materials and can be applied to quantum-ballistic bipolar electronic devices.

Acknowledgments

DH would like to acknowledge the financial supports from the Laboratory University Collaboration Initiative (LUCI) program and from the Air Force Office of Scientific Research

(AFOSR).

[1] A. Kara, H. Enriquez, A. P. Seitsonen, L. C. Lew Yan Voon, S. Vizzini, B. Aufray, and H. Oughaddou, Surf. Sci. Rep. **67**, 1 (2012).

[2] Z. Ni, Q. Liu, K. Tang, J. Zheng, J. Zhou, R. Qin, Z. Gao, D. Yu, and J. Lu, Nano Lett. **12**, 113 (2011).

[3] M. Dávila, L. Xian, S. Cahangirov, A. Rubio, and G. Le Lay, New J. Phys. **16**, 095002 (2014).

[4] L. Li, S.-Z. Lu, J. Pan, Z. Qin, Y.-Q. Wang, Y. Wang, G.-Y. Cao, S. Du, and H.-J. Gao, Adv. Mater. **26**, 4820 (2014).

[5] A. Acun, L. Zhang, P. Bampoulis, M. Farmanbar, A. van Houselt, A. Rudenko, M. Lingenfelder, G. Brocks, B. Poelsema, M. Katsnelson, et al., J. Phys.: Condens. Matt. **27**, 443002 (2015).

[6] L. Zhang, P. Bampoulis, A. van Houselt, and H. J. Zandvliet, Appl. Phys. Lett. **107**, 111605 (2015).

[7] P. Bampoulis, L. Zhang, A. Safaei, R. Van Gastel, B. Poelsema, and H. J. W. Zandvliet, J. Phys.: Condens. Matt. **26**, 442001 (2014).

[8] M. Derivaz, D. Dentel, R. Stephan, M.-C. Hanf, A. Mehdaoui, P. Sonnet, and C. Pirri, Nano Lett. **15**, 2510 (2015).

[9] C. Walhout, A. Acun, L. Zhang, M. Ezawa, and H. Zandvliet, J. Physics: Condens. Matt. **28**, 284006 (2016).

[10] A. K. Geim and K. S. Novoselov, Nature Mater. **6**, 183 (2007).

[11] K. S. Novoselov, A. K. Geim, S. Morozov, D. Jiang, M. Katsnelson, I. Grigorieva, S. Dubonos, and A. A. Firsov, Nature **438**, 197 (2005).

[12] Y. Zhang, Y.-W. Tan, H. L. Stormer, and P. Kim, Nature **438**, 201 (2005).

[13] C. R. Dean, A. F. Young, I. Meric, C. Lee, L. Wang, S. Sorgenfrei, K. Watanabe, T. Taniguchi, P. Kim, K. L. Shepard, et al., Nature Nanotechn. **5**, 722 (2010).

[14] C.-C. Liu, W. Feng, and Y. Yao, Phys. Rev. Lett. **107**, 076802 (2011).

[15] P. Vogt, P. De Padova, C. Quaresima, J. Avila, E. Frantzeskakis, M. C. Asensio, A. Resta, B. Ealet, and G. Le Lay, Phys. Rev. Lett. **108**, 155501 (2012).

[16] H. Xie, T. Ouyang, É. Germaneau, G. Qin, M. Hu, and H. Bao, Phys. Rev. B **93**, 075404 (2016).

[17] M. Ezawa, New J. Phys. **14**, 033003 (2012).

[18] B. Aufray, A. Kara, S. Vizzini, H. Oughaddou, C. Leandri, B. Ealet, and G. Le Lay, Appl. Phys. Lett. **96**, 183102 (2010).

[19] P. De Padova, C. Quaresima, C. Ottaviani, P. M. Sheverdyaeva, P. Moras, C. Carbone, D. Topwal, B. Olivieri, A. Kara, H. Oughaddou, et al., Appl. Phys. Lett. **96**, 261905 (2010).

[20] B. Lalmi, H. Oughaddou, H. Enriquez, A. Kara, S. Vizzini, B. Ealet, and B. Aufray, Appl. Phys. Lett. **97**, 223109 (2010).

[21] M. Ezawa, Phys. Rev. Lett. **109**, 055502 (2012).

[22] C.-C. Liu, W. Feng, and Y. Yao, Phys. Rev. Lett. **107**, 076802 (2011).

[23] C. J. Tabert and E. J. Nicol, Phys. Rev. B **87**, 235426 (2013).

[24] C. J. Tabert and E. J. Nicol, Phys. Rev. B **88**, 085434 (2013).

[25] C. J. Tabert and E. J. Nicol, Phys. Rev. B **89**, 195410 (2014).

[26] X. Wang, Y. Hong, P. K. Chan, and J. Zhang, Nanotechn. **28**, 255403 (2017).

[27] A. Feyzi and R. Chegel, Europ. Phys. J. B **89**, 193 (2016).

[28] N. Ma and D. Jena, Phys. Rev. X **4**, 011043 (2014).

[29] M. Kamatagi and N. Sankeshwar, in *AIP Conf. Proc.* (2015), vol. 1665, p. 110036.

[30] T. Gunst, T. Markussen, K. Stokbro, and M. Brandbyge, Phys. Rev. B **93**, 035414 (2016).

[31] C. Xiao, D. Li, and Z. Ma, Phys. Rev. B **93**, 075150 (2016).

[32] A. Lucas, J. Crossno, K. C. Fong, P. Kim, and S. Sachdev, Phys. Rev. B **93**, 075426 (2016).

[33] Y. Liu and P. P. Ruden, Phys. Rev. B **95**, 165446 (2017).

[34] P. Borowik, J.-L. Thobel, and L. Adamowicz, Semicond. Sci. Technol. **31**, 115004 (2016).

[35] V. Vargiamidis, P. Vasilopoulos, and G. Q. Hai, J. Phys.: Condens. Matt. **26**, 345303 (2014).

[36] V. Gusynin, S. Sharapov, and A. Varlamov, Phys. Rev. B **90**, 155107 (2014).

[37] M. Tahir, A. Manchon, K. Sabeeh, and U. Schwingenschlögl, Appl. Phys. Lett. **102**, 162412 (2013).

[38] L. Stille, C. J. Tabert, and E. J. Nicol, Phys. Rev. B **86**, 195405 (2012).

[39] L. Falkovsky and A. Varlamov, The European Physical Journal B **56**, 281 (2007).

[40] L. Falkovsky, Journal of Experimental and Theoretical Physics **106**, 575 (2008).

[41] S. K. Lyo and D. H. Huang, Phys. Rev. B **64**, 115320 (2001).

[42] S. K. Lyo and D. H. Huang, Phys. Rev. B **68**, 115317 (2003).

[43] S. K. Lyo and D. H. Huang, Phys. Rev. B **73**, 205336 (2006).

[44] E. Hwang, S. Adam, and S. D. Sarma, Phys. Rev. Lett. **98**, 186806 (2007).

[45] S. Adam, E. Hwang, and S. D. Sarma, Physica E: Low-dimensional Systems and Nanostructures **40**, 1022 (2008).

[46] S. D. Sarma, S. Adam, E. Hwang, and E. Rossi, Rev. Mod. Phys. **83**, 407 (2011).

[47] K. Bolotin, K. Sikes, J. Hone, H. Stormer, and P. Kim, Phys. Rev. Lett. **101**, 096802 (2008).

[48] Y. M. Zuev, W. Chang, and P. Kim, Phys. Rev. Lett. **102**, 096807 (2009).

[49] S. D. Sarma, E. Hwang, and E. Rossi, Phys. Rev. B **81**, 161407 (2010).

[50] S. D. Sarma and E. Hwang, Phys. Rev. Lett. **83**, 164 (1999).

[51] A. Iurov, G. Gumbs, D. H. Huang, and G. Balakrishnan, Phys. Rev. B **96**, 245403 (2017).

[52] D. H. Huang, C. Rhodes, P. M. Alsing, and D. A. Cardimona, J. Appl. Phys. **100**, 113711 (2006).

[53] D. H. Huang, G. Gumbs, and O. Roslyak, Phys. Rev. B **83**, 115405 (2011).

[54] V. Y. Tsaran, A. Kavokin, S. Sharapov, A. Varlamov, and V. Gusynin, Sci. Rep. **7**, 10271 (2017).

[55] A. Iurov, G. Gumbs, and D. H. Huang, J. Phys.: Condens. Matt. **29**, 135602 (2017).

[56] E. V. Gorbar, V. P. Gusynin, V. A. Miransky, and I. A. Shovkovy, Phys. Rev. B **66**, 045108 (2002).

[57] E. H. Hwang and S. Das Sarma, Phys. Rev. B **79**, 165404 (2009).

[58] S. Das Sarma and Q. Li, Phys. Rev. B **87**, 235418 (2013).

[59] B. Wunsch, T. Stauber, F. Sols, and F. Guinea, New J. Phys. **8**, 318 (2006).

[60] P. Pyatkovskiy, J. Phys.: Condens. Matt. **21**, 025506 (2008).

[61] B. Van Duppen, P. Vasilopoulos, and F. Peeters, Phys. Rev. B **90**, 035142 (2014).

[62] P. F. Maldague, Surf. Sci. **73**, 296 (1978).

[63] A. Scholz, T. Stauber, and J. Schliemann, Phys. Rev. B **88**, 035135 (2013).

[64] L. A. Falkovsky, in *J. Phys.: Conf. Series* (2008), vol. 129, p. 012004.

[65] L. A. Falkovsky, Physics-Uspekhi **51**, 887 (2008).

[66] L. Falkovsky and S. Pershoguba, Phys. Rev. B **76**, 153410 (2007).

[67] K. F. Mak, M. Y. Sfeir, Y. Wu, C. H. Lui, J. A. Misewich, and T. F. Heinz, Phys. Rev. Lett. **101**, 196405 (2008).

[68] A. Iurov, D. H. Huang, G. Gumbs, W. Pan, and A. A. Maradudin, Phys. Rev. B **96**, 081408 (2017).

[69] V. Gusynin and S. Sharapov, Phys. Rev. B **73**, 245411 (2006).

[70] A. Singh, K. I. Bolotin, S. Ghosh, and A. Agarwal, Phys. Rev. B **95**, 155421 (2017).

[71] J. P. Carbotte, J. P. F. LeBlanc, and E. J. Nicol, Phys. Rev. B **85**, 201411 (2012).

[72] A. Scholz and J. Schliemann, Phys. Rev. B **83**, 235409 (2011).

[73] A. Iurov, G. Gumbs, D. H. Huang, and V. Silkin, Phys. Rev. B **93**, 035404 (2016).

[74] T. Stauber, N. M. R. Peres, and A. K. Geim, Phys. Rev. B **78**, 085432 (2008).

[75] Z. M. Ziman, *Principles of the Theory of Solids* (Press Syndicate of the University of Cambridge, 1972).

[76] E. H. Hwang and S. Das Sarma, Phys. Rev. B **77**, 195412 (2008).

[77] T. Ando, J. Phys. Soc. Japan **75**, 074716 (2006).

[78] O. Kibis, Phys. Rev. B **81**, 165433 (2010).

[79] K. Kristinsson, O. Kibis, S. Morina, and I. Shelykh, Sci. Rep. **6**, 20082 (2016).